Accelerated MINFLUX Nanoscopy, through Spontaneously Fast-Blinking Fluorophores

Michael Remmel, Lukas Scheiderer, Alexey N. Butkevich, Mariano L. Bossi,* and Stefan W. Hell*

The introduction of MINFLUX nanoscopy allows single molecules to be localized with one nanometer precision in as little as one millisecond. However, current applications have so far focused on increasing this precision by optimizing photon collection, rather than minimizing the localization time. Concurrently, commonly used fluorescent switches are specifically designed for stochastic methods (e.g., STORM), optimized for a high photon yield and rather long on-times (tens of milliseconds). Here, accelerated MINFLUX nanoscopy with up to a 30-fold gain in localization speed is presented. The improvement is attained by designing spontaneously blinking fluorescent markers with remarkably fast on-times, down to 1–3 ms, matching the iterative localization process used in a MINFLUX microscope. This design utilizes a silicon rhodamine amide core, shifting the spirocyclization equilibrium toward an uncharged closed form at physiological conditions and imparting intact live cell permeability, modified with a fused (benzo)thiophene spirolactam fragment. The best candidate for MINFLUX microscopy (also suitable for STORM imaging) is selected through detailed characterization of the blinking behavior of single fluorophores, bound to different protein tags. Finally, optimization of the localization routines, customized to the fast blinking times, renders a significant speed improvement on a commercial MINFLUX microscope.

1. Introduction

Super-resolution fluorescence microscopy (nanoscopy) afforded the all-optical visualization of specimen details much finer than the ≈250 nm diffraction resolution limit.[1] The first generation of these techniques (stimulated emission depletion microscopy (STED), reversible saturable optical fluorescence transitions microscopy (RESOLFT), photo activated localization microscopy (PALM), stochastic optical reconstruction microscopy (STORM), point accumulation for imaging in nanoscale topography (PAINT)),[2–7] can routinely achieve a resolution down to 20–50 nm, enabling the detailed visualization of submicrometer-size cellular structures in living cells.[8] While they all use two distinct fluorophore states for telling neighboring fluorophores apart (typically a fluorescent "on" and a dark "off" state), nanoscopy methods differ in the spatio-temporal control of the "on" and "off" states and the way the position of the fluorophore is established in the sample. The coordinate-stochastic single-molecule methods called PALM, STORM, and PAINT infer these positions from the diffraction pattern of the fluorescence light rendered by single fluorophores on a pixilated detector such as a camera. In contrast, the coordinate-targeted methods STED and RESOLFT scan the sample with a spatially modulated illumination pattern with a minimum intensity node (ideally zero) that defines a reference position for the markers. In single beam scanning implementations this pattern is typically shaped like a donut. By synergistically using the unique advantages of both strategies, the recently introduced MINFLUX (MINimal photon FLUXes) concept pushes the fluorescence nanoscopy resolution down to a few nanometers.[9] Concretely, MINFLUX separates neighboring fluorophores by on/off-switching their emission capability individually, like PALM or STORM, but localizes the emitting fluorophore with a pattern of excitation light featuring an intensity node, like the donut used in STED microscopy.[10] Localization with a donut-shaped excitation beam shifts the burden of requiring many photons for localization on the excitation beam, so that the number of fluorescence photons required for attaining a certain localization precision or speed is substantially reduced.[9] Minimizing the required number of detected photons lessens the demand on the on/off-switchable fluorophores regarding brightness in the "on"-state and photostability. Thus, the possible range of viable fluorescent molecular switches and switching mechanisms is expanded over that used in established PALM and STORM techniques.

M. Remmel, L. Scheiderer, S. W. Hell
Department of Optical Nanoscopy
Max Planck Institute for Medical Research
Jahnstrasse 29, 69120 Heidelberg, Germany
E-mail: Stefan.Hell@mpinat.mpg.de
A. N. Butkevich, M. L. Bossi, S. W. Hell
Department of NanoBiophotonics
Max Planck Institute for Multidisciplinary Sciences
Am Fassberg 11, 37077 Göttingen, Germany
E-mail: mariano.bossi@mr.mpg.de

The ORCID identification number(s) for the author(s) of this article can be found under https://doi.org/10.1002/smll.202206026.

**ADVANCED
SCIENCE NEWS**

www.advancedsciencenews.com

**NANO · MICRO
small**

www.small-journal.com

In principle, the fluorophores that work for PALM and STORM, such as cyanine dyes,[11,12] or caged rhodamines[13] also work for MINFLUX microscopy.[9,14–17] Yet, as they are optimized for the detection of isolated fluorescence patterns on a camera, typical PALM/STORM fluorophores do not necessarily leverage the specific advantages provided by MINFLUX in terms of attainable resolution and, particularly, speed. Markers are designed to have an on-time (T_{ON}) preferably matching the frame-rate of the camera ($T_{ON} \approx$ frame-rate$^{-1} \approx$ 10–20 ms), and to provide a large number of detected photons (typically N_{PH} = 1000–5000) during the on-time. In contrast, MINFLUX requires less than a tenth of that number of photons to achieve the same resolution[9] and can localize emitters in time intervals below a millisecond.[18] Besides, most common classes, cyanine and caged triarylmethane fluorophores entail unfavorable conditions. For example, the blinking behavior of cyanines requires complex redox buffers, comprising an enzymatic system and several chemicals (thiols or reducing agents).[19] Thus they are incompatible with live-cell imaging and their imaging conditions may affect other markers or functional biomolecules. It is widely recognized that the imaging buffer affects the image quality. Therefore, a wide variety of buffer compositions[20–24] have been used; some of them are even undisclosed. Despite their successful use in super-resolution techniques for more than a decade, the physicochemical mechanism of the blinking behavior is still debated.[20,25,26] While caged fluorophores have simpler, more reliable, and usually known activation mechanisms (on-switching),[27–33] their off-switching (with rate k_{OFF} = $1/T_{ON}$) relies on complex and poorly defined photobleaching reactions. Moreover, their activation can be induced by the excitation laser (in a one or two-photon process), and the photoactivation products (rhodamine dyes) are prone to oxidative photobluing.[34] Finally, the reaction kinetics of both on- and off-switching of cyanines and caged fluorophores strongly depend on the irradiation wavelength and intensity. Alternatively, fluorophores whose blinking is induced solely by thermal reactions become an appealing choice. While the use of such spontaneous blinking or self-blinking dyes is well established in STORM and related methods,[35–47] their exploitation in MINFLUX[48] is still uncharted. Based on their simplicity, resulting from a switching process involving only ground states, we deemed these systems as more suitable scaffolds to build fluorescent markers with desired properties.

Here, we present accelerated MINFLUX nanoscopy, based on the combination of optimized localization schemes, along with the design of customized spontaneous blinking fluorophores with fast on-times, tailored to match the localization speed requirements. As the vast majority of markers utilized so far have been optimized for camera-based detection methods, their long on-times of typically 10–50 ms are far from optimal for MINFLUX. Thus, we first synthesized and characterized a series of spontaneously blinking fluorescent labels based on a reversible spirocyclization of silicon rhodamine amides, specifically designed to achieve considerably shorter on-times ($T_{ON} < 10$ ms). We carried out a systematic study of their blinking behavior at the single-molecule level, with particular emphasis on the relevant characteristics for MINFLUX nanoscopy. Although the demand on detected photons (N_{PH}) is not severe, high brightness is still necessary to compensate

for the reduction in the burst duration (i.e., emission rates in the ON-state should still be high [N_{PH} = rate $\times$ T_{ON}]). In addition, duty cycles (DC = $T_{ON}/([T_{ON} + T_{OFF}])$) must be kept low as the blinking process imposes a limit on the maximum number of distinguishable markers in a diffraction-limited light spot. This in turn limits the translation of localization accuracy into the final resolution of the image,[49] as a fluorescence microscope images fluorophores rather than the structures (or biomolecules) to be resolved. However, the DC must also not be too low, to ensure a reasonable frequency of blinking events, and avoid unnecessarily prolonged total imaging times. We noted that the overall blinking behavior of the fluorophore is affected by the nature of the labeled biomolecule (protein) used for targeting desired structures. This is consistent with the effects of the local environment on the spirocyclization equilibrium. MINFLUX performance, as well as other super-resolution microscopies, rely and strongly depend on the switching behavior. Thus, this emphasizes the importance of the selection of appropriate tagging or labeling methods for new or existing markers. We prepared reactive adducts for their application with common fixed- and live-cell labeling strategies, bioconjugates (nanobodies) and a self-labeling enzyme (HaloTag). Paying particular attention to the attainable localization efficiency, speed, and analyzing the influence of the blinking properties on the image quality, we identified the best candidate. Finally, we imaged nuclear pore complexes (NUPs) in U2OS cells with a fluorophore localization precision less than 3 nm, using a commercially available MINFLUX microscope.

2. Results and Discussion

2.1. Design and Synthesis of Spontaneously Blinking Fluorophores for Fast Minflux

The majority of reported spontaneously-blinking fluorescent labels are derived from a rhodamine core. Rhodamine dyes afford brightness and photostability, a wide spectral range (green to near-IR emission, with excitation from 488 to 640 nm) and a relatively simple and well-documented synthetic chemistry.[50] While they are also capable of intramolecular spirocyclization between their electrophilic xanthylium chromophore and the 2′-carboxylate nucleophile to form a colorless and non-emissive lactone, in polar environments the equilibrium is largely shifted toward the emissive zwitterionic form. Bearing a stronger 2′-carboxamide nucleophile, the corresponding rhodamine amides exist nearly exclusively in the form of colorless spirolactams. As the thermal blinking of these early rhodamine spirolactams is inefficient at physiological pH, STORM imaging has been carried out with these dyes by photoactivation.[51,52] Custom chemical design yielded spontaneously blinking derivatives of 2′-(hydroxymethyl)silicorosamine (HMSiR),[37] sparing 355–405 nm UV photoactivation. In further reports, both expansion of the spectral range[53] and rational tuning of their blinking behavior[54] were reported for this class of fluorophores.

In our design, we started from the silicon rhodamine (SiR) core structure, because the excitation and emission of SiR

**ADVANCED
SCIENCE NEWS**
www.advancedsciencenews.com

NANO · MICRO

small
www.small-journal.com
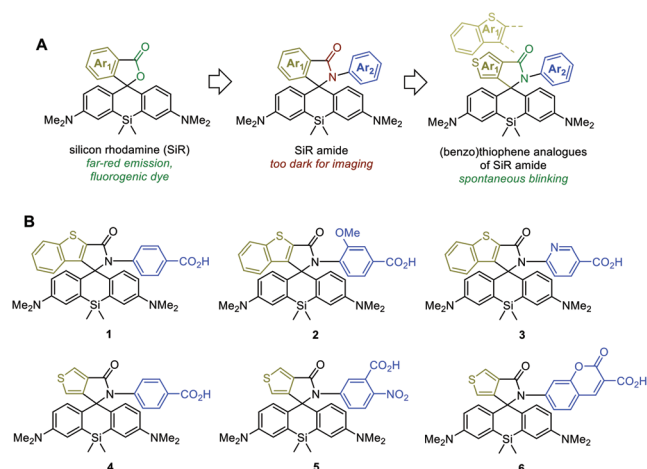
Scheme 1. A) Design of spontaneously blinking fluorophores derived from silicon rhodamine (SiR) and based on the silicon rhodamine amide core; B) Chemical structures of the six blinking fluorophores synthesized in this work.

dyes in the red spectral region matches the 640 nm laser line of commercial microscopes. Red light also minimizes background in cell imaging, keeps photodamage and light dispersion at bay, and increases cell and tissue penetration. However, the amido derivatives of the SiR dye itself (**Scheme 1**A) do not undergo spirolactam ring opening in aqueous buffers. To shift this equilibrium toward the open form and tune the blinking behavior, we explored a series of SiR-derived amides with varying Ar_1 and Ar_2, following the strategy that has been successfully used to optimize the fluorogenicity and cell membrane permeability of a series of rhodamine derivatives.[46,53,55,56]

Replacement of a fused benzene ring in the spirolactam core (Ar_1) with a thiophene or a benzothiophene was aimed at increasing the angle strain in the resulting [3.3.0] bicyclic ring system of the spirolactam unit (compared to the [4.3.0] system of SiR dye), disfavoring the spirocyclization. This resulted in the desired spontaneous blinking behavior with a far-red (680–690 nm) fluorescent emission (**Figure S1**, Supporting Information) of the reference dyes **1** and **4** (Scheme 1B). Further tuning of the electronic properties of the *N*-amido substituent (Ar_2) allowed the necessary control over K_{a2} equilibrium constant (**Figure 1**B)[57,58] and, as a result, over the extent of spirolactam ring opening in neutral aqueous buffer and the characteristics of the stochastic blinking.

Compounds **1–6** (Scheme 1B) were prepared from the corresponding SiR lactones with modified fused aromatic ring, which were converted to the corresponding acyl chlorides upon treatment with oxalyl chloride or phosphorus(V) oxychloride and condensed with the appropriately substituted 3- or 4-aminobenzoic acid ester (7-aminocoumarin derivative for **5**). Free carboxylic acid forms of the dyes **1–6** were recovered by mild acidic or basic hydrolysis (see Supporting Information for the experimental details). Further functionalization of the carboxylic acid provided the amino-reactive *N*-hydroxysuccinimide (NHS) esters, thiol-reactive maleimide derivatives and self-labeling HaloTag protein (an engineered ω-chloroalkyl dehalogenase[59]) ligands.
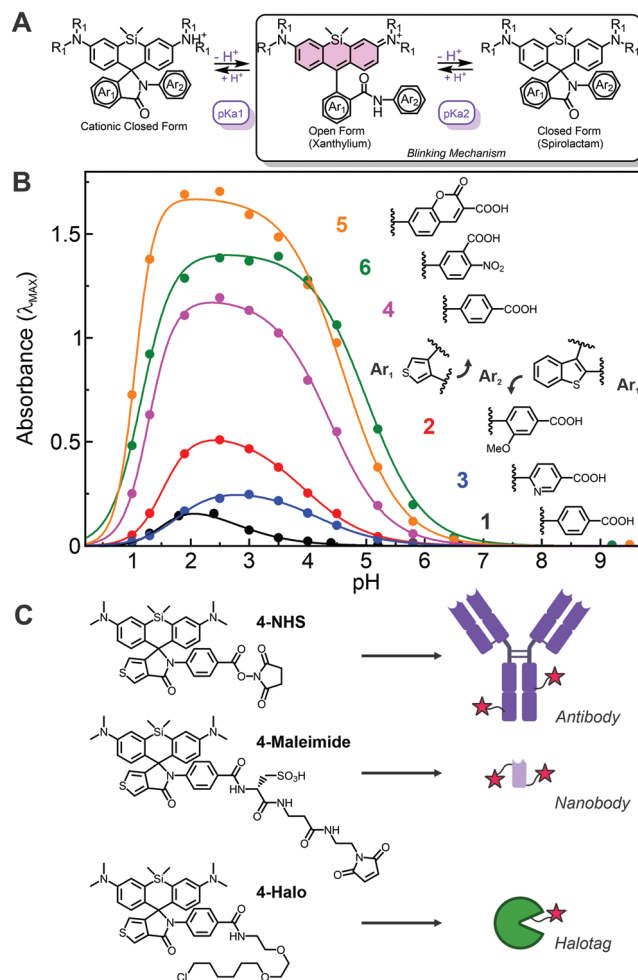

Figure 1. A) General structure of the studied fluorophores and the reactions responsible for their blinking behavior; B) pH dependence of the red absorption band of the closed form and the structures of the substituents Ar_1 and Ar_2 for each compound (dots: measurements; lines: fits according to the model described in the Experimental Section); C) reactive adducts (NHS, maleimide, chloroalkane) and schematic representation of the labeling strategies (antibodies, nanobodies, and self-labeling enzyme HaloTag) for the corresponding reactive adduct of compound **4** (red stars).

2.2. Ensemble Characterization of Carboxylic Acids 1–6 in Solution

We first studied the absorption and emission properties of the six compounds in a buffered solution at pH = 7.4 (**Figure S1**, Supporting Information). The effect of Ar_2 substituent pattern on the spectral properties was minimal, with maximum absorption and emission variability within 10 nm. The emission efficiency also shows small changes (**Table 1**), with benzothiophene derivatives demonstrating decreased fluorophore brightness. On the contrary, considerable variations were observed in response of the spirolactam–xanthylium amide equilibrium to the change of pH (Figure 1 and Figure S2, Supporting Information), with the spirolactam form predominant in neutral and basic environments, and the xanthylium in moderately acidic media (corresponding to pK_{a2}, see Figure 1A and Table 1). This

**ADVANCED
SCIENCE NEWS**

www.advancedsciencenews.com

NANO · MICRO

small

www.small-journal.com

equilibrium is more shifted toward the spirolactam closed form for Ar_1 = benzothiophene than for Ar_1 = thiophene. Within each group, varying the electronic properties of Ar_2 results in the fine-tuning of the equilibrium. Below pH = 2, a second colorless and non-emissive form becomes prevalent for all compounds, suggesting a second protonation step corresponding to pK_{a1}. While this behavior was observed for some rhodamine amides[53] and HMSiR analogues,[39,60] it has not been described for SiR-amide derivatives.[46,57] The proposed species and involved equilibria are shown in Figure 1A. Based on this simplified representation, the two equilibrium constants were extracted by fitting the absorbance at the maximum of the xanthylium form with a Hill's model.[61] It is noteworthy that all compounds predominantly exist in the spirocyclic closed form (SP, Figure 1A) at physiological pH values. This neutral form is known to be cell permeable for similar rhodamines and silicon rhodamines.

2.3. Single Molecule Characterization

The presence of two separate prototropic equilibria and the proximity of the values K_{a1} and K_{a2} makes it difficult to corroborate if there exists a pH interval within which any of the SiR-amides **1–6** is present solely in the xanthylium form. For this reason, the molar absorption coefficients of the colored form could not be reliably calculated. Moreover, the absorption of dyes **1–6** is too low and close to the instrument noise levels at neutral pH, so duty cycles below 10^{-3} are expected. It was therefore deemed practical to evaluate these parameters by studying the blinking properties at the single molecule level. First, full IgG secondary antibodies were treated with reactive NHS ester derivatives of **1–6** (Figure 1C) to a low degree of labeling (≤0.3) to minimize the probability of tagging a single protein with more than one blinker. The antibodies were affixed to a cover slide based on a streptavidin/biotin double recognition system (Figure S3, Supporting Information), whose extremely high affinity prevents any detachment of the antibodies for even longer times than those required for the experiment. Concentrations and incubation times were optimized to ensure a sparse surface distribution of the antibodies labeled with blinking fluorophores. Finally, samples were mounted in PBS and imaged on a custom-made microscope allowing for wide-field (camera-based) and confocal detection. With the first, parallel data collection (≈30 molecules in a 12 × 12 µm area) was achieved with 10 ms temporal resolution, and with the second one a higher time-resolution of 1 ms was reached. Excitation intensity was the same in both modalities, and approximately matched the values necessary for imaging in a MINFLUX microscope (66 kW cm^{-1},[2] calculated in the sample's plane). Due to the large difference in the characteristic times of the two processes (on- and off-switching), we extracted T_{OFF} from wide-field experiments and T_{ON} from confocal measurements. However, the analysis procedure for the data from single molecule traces was the same in both cases (Figures S4–S7, Supporting Information). The data is summarized in **Table 1** and Table S1, Supporting Information, along with other relevant calculated parameters. Since not all molecules are bleached at the end of the experiment, calculated number of cycles (N_{CY}) should be considered a lower limit.

In general, benzothiophene-derived spirolactams **1–3** demonstrate shorter on-times and longer off-times (and therefore a lower duty cycle) than thiophene derivatives **4–6**. While T_{ON} and T_{OFF} under neutral conditions do not have a clear correlation with the equilibrium constant K_{a2} corresponding to the reversible spirocyclization, a reasonable correlation was observed for the DC within each group (**Figure 2**). The T_{OFF} parameter demonstrates larger variation than T_{ON} and thus has a stronger effect on the DC. Compared to other blinking fluorophores used in super-resolution techniques (including cyanines),[21] the DC of compounds **1–6** lies in the same range of 10^{-3}–10^{-4}. Such low values are known to be compatible with stochastic methods[6,21] and MINFLUX[9,17] imaging with high labeling density. In addition, we found no observable changes in T_{OFF} upon illuminating the sample with UV light of 405 nm with intensities up to 1 kW cm^{-1}.[2] We therefore dismiss a potential contribution of a photo-induced activation/on-switching mechanism under our conditions (aqueous environment, pH = 7.4, irradiation wavelength and power). With respect to the DC, there is little information in the literature of spontaneously blinking fluorophores to compare.[36,37,39,41–43,46,49] Regarding on-times, compounds **1–6** present DC values that are in general 1 to 2 orders of magnitude shorter than for previously reported compounds (Figure S6, Supporting Information).[37,38,42,46] They also present non-mono-exponential behavior: after fitting to a bi-exponential model, we found a predominant short T_{ON} component at the

Table 1. Photophysical properties of compounds 1–6. Φ_{Fluo}: fluorescence quantum yield of the emissive form; $Ka_{1,2}$ and $n_{1,2}$: equilibrium constants and the corresponding Hill's coefficients extracted from the fit described in the Experimental Section; DC: duty cycle; $T_{ON}/(T_{ON}+T_{OFF})$: on- and off-times; N_{CY}: average number of cycles per trace; %Bl: percentage of molecules bleached (upper limit); PH_{CY}: average number of photons detected per cycle (on-time); Rate: emission rate.

Dye	Φ_{Fluo}	n_1	pKa_1	n_2	pKa_2	K_{eq}	DC ×10^3	T_{ON} [ms]	T_{OFF} [s]	N_{CY}	%Bl	PH_{CY}	Rate [kHz]
1	0.10	1.70	1.62	0.79[a]	2.62	417	0.31	1.3	4.25	13	45	143	111
2	0.17	1.52	1.52	—	3.92	8318	0.39	2.1	5.37	7	62	251	120
3	0.24	1.77	1.77	—	4.17	14 791	0.93	1.2	1.30	36	53	115	96
4	0.16	1.28	1.28	0.90[a]	4.38	23 988	2.89	3.0	1.02	14	86	354	118
5	0.17	1.05	1.05	—	4.60	39 811	3.46	1.9	0.56	39	78	207	109
6	0.16	1.28	1.28	—	5.00	100 000	5.28	2.6	0.50	58	71	278	107

[a]A global fit was used for each group.

**ADVANCED
SCIENCE NEWS**

www.advancedsciencenews.com
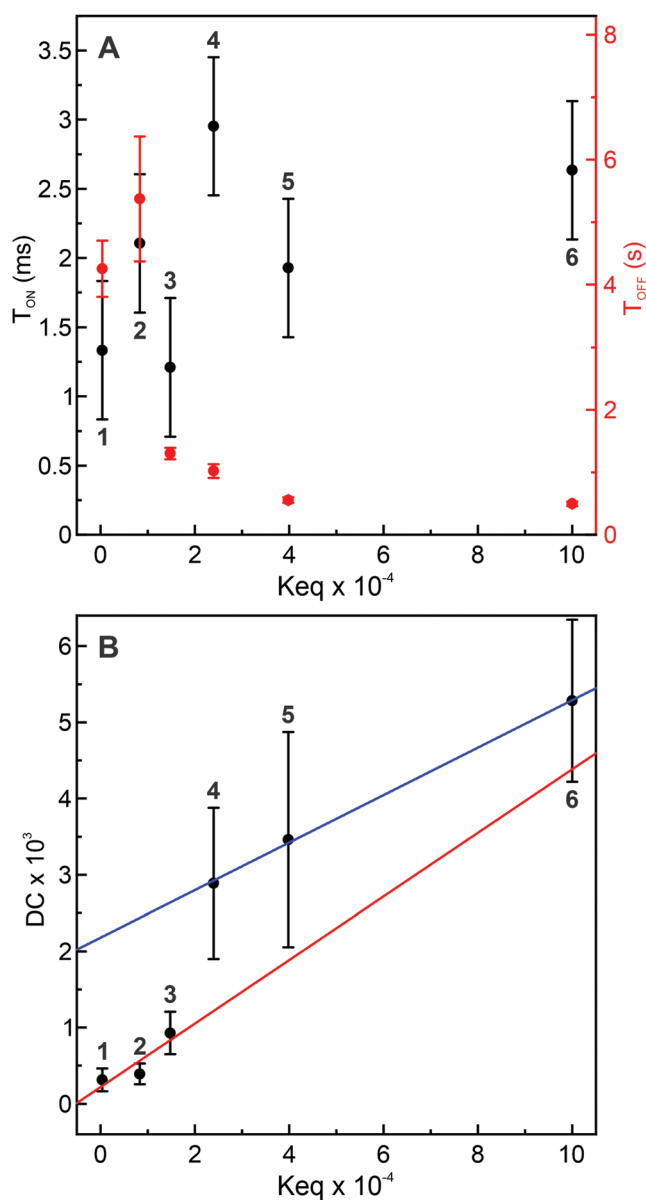
**NANO · MICRO
small**

www.small-journal.com

Figure 2. A) Average on-times (T_{ON}), off-times (T_{OFF}), B) and the resulting duty cycle (DC) measured from single molecule traces of antibodies labeled with compounds 1–6 with a low degree of labeling (DOL ≤0.3), as a function of the equilibrium constant ($K_{eq} = 1/K_{a2}$). A linear regression is plotted for each group of compounds (1–3: Ar$_1$ = benzothiophene, 4–6: Ar$_1$ = thiophene).

than that of benzothiophenes **1–3**). In this group, we selected the compound **4** with a slightly longer T_{ON} than the others. Next, three distinct tags, commonly employed for labeling biological samples, were selected (Figure 1C): NHS ester for tagging free primary amino groups of secondary antibodies (for imaging purposes, higher DOLs ≈2–3 were prepared), maleimide for selective modification of cysteine residues in engineered nanobodies, and linear ω-chloroalkane with a short PEG2 linker for labeling HaloTag fusion proteins. In the case of nanobodies, we have noticed that several hours post-labeling with the hydrophobic dyes, significant aggregation and precipitation of the tagged protein from the aqueous solution makes their application impractical. This solubility problem was solved by the introduction of an additional hydrophilic dipeptide linker (Cya-β-Ala, termed a "universal hydrophilizer"),[62] obtaining complete labeling to a defined DOL of 2 (Figure S10A, Supporting Information). To confirm the covalent binding of a HaloTag ligand to its target fusion protein, ESI mass spectroscopy of a labeled HaloTag7 sample was performed (Figure S10B, Supporting Information). The blinking behavior of fluorophores in these biomolecular complexes was also studied (Figure S7 and Table S1, Supporting Information) and compared with the correspondingly labeled antibody. We also confirmed their suitability for STORM imaging (Figure S11, Supporting Information). We observed a considerable influence of the environment on the on- and off-times and therefore on the resulting duty cycle, especially for the HaloTag conjugate. To our knowledge, there is not much information in the literature regarding the effects of labeling on the duty cycle of blinking fluorophores, probably because of the marginal effect on imaging with a camera detector, given the long exposure times (typically >10 ms). However, we expect a larger impact on MINFLUX imaging, in particular when applying much shorter localization times (≤10 ms). Intrigued by the non-mono-exponential behavior, we then decided to inspect the on-times in detail. While a bi-exponential model fits the data and allows calculation of average on-times, a bimodal distribution may not be an adequate physical description of the system, with rather complex microenvironments affecting the fluorophore. We found a better comparison by a model-independent analysis of the experimental complementary cumulative distribution function (CCDF) of T_{ON} (**Figure 3**). In the first place, we observed an initial drop of 50–65% that accounts for the fraction of $T_{ON} \leq$ 1 ms. These are probably discarded in camera-based localization methods (because of low photon numbers or signal-to-background level), but can be potentially localized in MINFLUX; this will be discussed in the next section. Another large group of T_{ON}'s (≈20%) is in the range of 5–50 ms; we attribute the suitability of compounds **1–6** for STORM imaging to this fraction of blinking events.

2.4. MINFLUX Imaging

To show their suitability for MINFLUX imaging, we labeled mEGFP-Nup107 cells with **4** linked to an anti-GFP nanobody through a hydrophilic linker and U2OS-Nup96-Halo cells with **4-Halo** ligand. NUPs have been previously proposed and used as a benchmark for super-resolution microscopy.[17,63] The

limit of the experimental temporal resolution (0.5–1 ms), and the long component with $T_{ON} \approx$ 3–10 ms. These are slightly shorter than the typical localization times used in MINFLUX microscopy,[16,17] and considered in principle relatively short for purely stochastic methods. Nevertheless, we obtained STORM images with fixed and live cells (Figures S8 and S9, Supporting Information) using immunostaining and HaloTag labeling, respectively. The latter also confirms the cell-permeability of HaloTag ligands derived from compounds **3–6**.

For MINFLUX imaging, we initially selected thiophene derivatives **4–6** for their larger DC (≈one order of magnitude larger

ADVANCED
SCIENCE NEWS
www.advancedsciencenews.com

NANO · MICRO
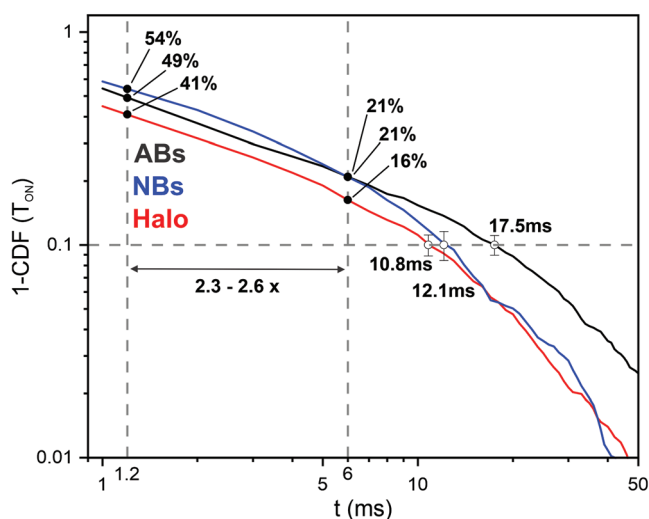**small**
www.small-journal.com

Figure 3. Complementary cumulative distribution function of T_{ON} for compound 4 measured in antibodies (black), nanobodies (blue), and bound to HaloTag7 (red). The values at 1.2 and 6 ms (the localization times of the imaging sequences used, see Table S2, Supporting Information), and the crossing points at 10% are marked for each case.

imaging was performed on a commercial MINFLUX setup without any instrumental modifications (see Section 4.8 of the Experimental Section for details). Initially, a standard MIN-FLUX sequence optimized for cyanine dyes (e.g., Alexa Fluor 647, Sulfo-Cy5, Biotium CF660 and CF680) and provided by the manufacturer was used. The localization process can be split in two parts (see Table S2, Supporting Information, for details). The first part consists of a series of 4 steps to pre-localize a molecule and progressively lower the MINFLUX localization range L;[9,16] it lasts 4 ms and requires at least a total of 120 photons above background. The second one consists of a pre-localization step ($L = 76$ nm) and the final localization step ($L = 40$ nm), rendering the position of the molecule. The dwell time is 2 ms (1 + 1 ms) and requires at least 30 photons per step. This second part is repeated as long as the molecule is in the on-state. Thus, each single molecule event (trace) results in a series of N_{LOC} localizations and a total number of photons N_{PH} over a locali-

zation time T_{LOC}. The localization precision is evaluated from the dispersion of the localization of all molecules around their corresponding mean position.[16–18] For both staining strategies, with anti-GFP nanobodies and HaloTag, we obtained MIN-FLUX images with compound 4, comparable to those previously reported with a similar setup (**Figure 4**).[17] Variabilities in the NUPs shape (ring-like structure, circularity, symmetry) have been discussed in the literature.[64] In our case, we attribute the main differences to a considerable variability in the fixation process. Without localization binning, a localization precision of $\sigma = 2.6$ nm/$\sigma = 2.9$ nm was reached (Figure 4B,D). From further analysis of the traces from Figure 4A, we estimated for each SM trace a median of 7 localizations, a total of 1300 photons (at a rate of 57 kHz) per molecule trace (185 photons per localization) for the nanobody. Similar values were found for the HaloTag image from Figure 4C (Table S3, Supporting Information). Previous work reported a localization precision below 1 nm calculated from traces with at least 4 localizations with 2100 photons per loc.[17] At an emission rate of 30 kHz, a molecule should persist in the on-state for at least 260 ms to be localized with such precision, corresponding to an average operative T_{LOC} (i.e., for blinking events effectively used to achieve such localization precision) of several hundreds of milliseconds (Table S3, Supporting Information). Gwosch et al.[16] also reported similar values. Since the on-time of cyanines is typically several tens to a few hundreds of milliseconds (power dependent),[26,27] a large fraction of blinking events will be localized unnecessarily multiple times. Compounds **1–6** have on-times in the range of few milliseconds, leaving a small fraction of fluorophores localizable in the on-state for more than 10–20 ms (Figure 3). From the distribution of the measured on-times (Figure 3 and Figure S7, Supporting Information), we conclude that images acquired with this standard ("slow") routine (Figure 4) result predominantly from the fraction of blinking events with the long T_{ON}. To evaluate the obtained localization precision, we binned the data presented in Figure 4, to compare with the precision values reported previously (Figure S12, Supporting Information). Binning with a set value of 350 photons, we reached a raw localization precision of 1.9 nm, which can be reduced to 1.1 nm after applying a filtering method (DBSCAN + outlier suppression, for details see Experimental
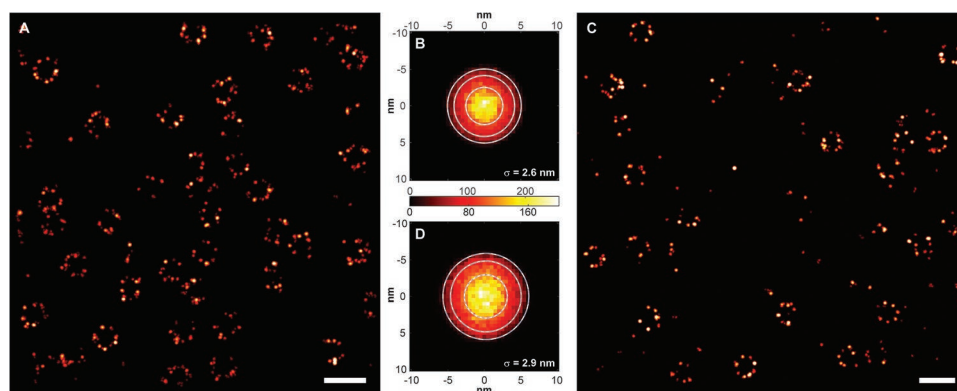

Figure 4. MINFLUX images of A) mEGFP-Nup107 fixed cells labeled with an anti-GFP nanobody (dye 4, DOL = 2), and C) U2OS-Nup96-Halo fixed cells labeled with 4-Halo (live-cell labeling and then fixed, see Experimental Section for details). B,D) The corresponding 2D dispersion plots (distance between localization and mean position of the cluster) are presented in (B) and (D), respectively. Scale bar: 200 nm.

ADVANCED
SCIENCE NEWS
www.advancedsciencenews.com

NANO · MICRO
small
www.small-journal.com

Section). However, binning the data acquired with our blinkers results in a loss of events (rejected due to a short T_{ON} and thus low N_{PH}), affecting the quality of the image.

These initial results showed that the spontaneously blinking fluorophore **4** could be successfully used in MINFLUX imaging and required a total acquisition time similar to previously reported values for cyanine labels. However, the imaging sequence used did not take advantage of the full potential of our dyes as fast blinkers. In fact, setting a high bar on the total photon budget (up to 8000) is at the expense of localization speed (up to several hundreds of milliseconds per localization, on average) and bears the risk of fluorophore dislocation. The precision required for discerning single biomolecules ($\approx$2–4 nm, the size of many proteins such as GFP, HaloTag or a nanobody) can be achieved with much fewer photons (<100) in MINFLUX.[9] Keeping an eye on localization speed, we decided to adapt the MINFLUX sequence to the photophysical properties of our fast blinkers (in particular their short on-times) and make use of a larger fraction of blinking events with short on-times. The main optimizations of the MINFLUX imaging routine were: 1) lowering the pre-localization time from 4 to 0.7 ms by reducing the number of steps from 4 to 2 and the localization time from 2 to 0.5 ms, and 2) increasing the localization range L from 40 to 76 nm for the localization step. With these modifications, the minimum time required to localize a molecule was reduced from 6 to 1.2 ms. To compensate for the loss

of photons, the excitation intensity was increased by a factor of 2, to a value close to the maximum of the laser power available in the commercial microscope. Overall, we expected a trade-off in spatial resolution (particularly due to a $\approx$2× increase in L) for a fivefold increase in localization speed and the fraction of blinking events used.

An image acquired with the optimized sequence ("fast"), directly compared with the "slow" sequence image (both at the same excitation power) is presented in **Figure 5** (a temporal image buildup is shown in Figure S13, Supporting Information), for mEGFP-Nup107 labeled with anti-GFP nanobodies labeled with dye **4**. The emission rate of the fluorophores was enhanced to 76 and 118 kHz for the slow and the fast sequence, respectively. An average value of 314 and 75 photons/localization was obtained, resulting in a localization precision of 2.3 and 3.7 nm, respectively (Table S3, Supporting Information). This moderate loss of resolution (by a factor of 1.6) is accompanied with a 5–7-fold increase in the effective average localization speed (Table S3, Supporting Information, T_{LOC}) and improved localization efficiency. The latter can be concluded from the total events on the images on Figure 5, normalized by the numbers of NUPs, showing a $\approx$2.6-fold increase for the fast sequence. Moreover, the cumulative distribution function shows that 90% of the traces were acquired with the fast sequence within 42 ms (on T_{LOC} distribution), closer to the 12 ms (on T_{ON} distribution) obtained from single molecule
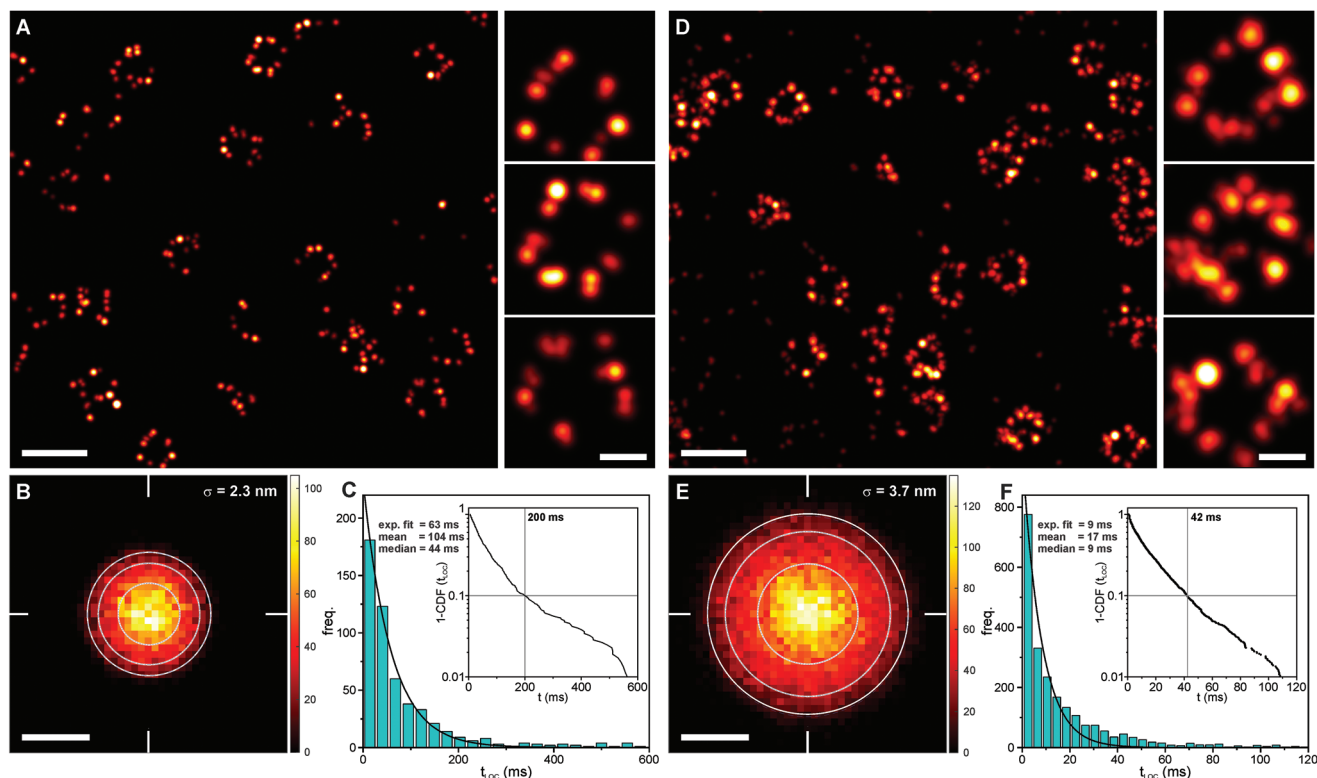

Figure 5. MINFLUX images of mEGFP-Nup107 cells labeled with nanobodies tagged with dye 4 (DOL = 2), A) with a 6 ms/iteration "slow" sequence, and D) with a 1.2 ms/iteration "fast" sequence. Selected individual NUPs are shown at the bottom of the panels. B,E) 2D dispersion plots (a distance between the localization and the mean position of the cluster) were fitted with a 2D Gaussian, and mean sigma value is indicated, along with circles of 1×, 1.64×, and 2×σ. C,F) Histograms for T_{LOC} ($\Delta t = t_{LAST} - t_{FIRST}$) are also presented, with the experimental cumulative distribution function (the indicated value corresponds to 90% of the events). Scale bars: (A,D) 200 nm (inset: 50 nm); (B,E) 5 nm.

characterizations (compare Figures 5 and 3). We attribute this difference to three distinct effects. First, at least a minimum of 2 localizations per molecule, plus the pre-localization, are necessary (see Supporting Information), limiting our time resolution to 1.7 ms as compared to 1 ms in the single molecule experiments. Second, despite approximate matching of the total excitation intensity between experiments, the fluorescent molecule experiences a variable effective value (probably lower) as it is moved near the nodal point in the imaging experiment. Longer blinking events producing larger detection numbers are favored, pushing the observed T_{LOC} to larger values. Finally, despite our best efforts to maintain the same molecular microenvironment in the characterization and imaging experiments, small differences cannot be excluded. Compared to previous work based on cyanine fluorescent labels, we increased the speed of localizations by a factor of 20–30× with only a 2–4-fold decrease in localization precision.[17] Nevertheless, the final localization precision of our fast (optimized) sequence is still below the typical size of the protein tags.

To compare whether a cyanine marker also profits from the fast localization routine, we imaged cells stained with Alexa Fluor 647-BG on NUP107-Snap cells[64] (Figure S14, Supporting Information) with both imaging sequences (Table S2, Supporting Information). Imaging with the slow standard routine results in images of good quality, with an average localization time of 76 ms (σ = 2.9 nm, emission rate = 43 kHz). Localizing Alexa Fluor 647 via the fast routine is possible (σ = 4.0 nm, emission rate = 76 kHz), but shows a notable loss of image quality (compare final images, at 35 min), beyond the expected loss in localization precision ascribed to the twofold increase in L. In addition, overall imaging speed was not improved. Images recorded with dye **4** are close to completion after 5–10 min, while those with Alexa Fluor 647 visibly require longer times (35 min). Surprisingly, the average localization time of Alexa Fluor 647 was substantially reduced while imaging with the fast routine to 12 ms, despite excitation and activation powers were identical. We hypothesize that the main reason for this effect is an inefficient localization that results in artificial splitting of SM traces (i.e., when localizations belonging to a single emitter are assigned as two or more traces, thus as different SM emitters), shrinking T_{LOC}, and result in a large fraction of off-target localizations observable in the image accounting for a poorer quality. Increasing the emission rate for a sufficient number of photons per localization yielded an even inferior image quality, possibly due to bleaching. This confirms that Alexa Fluor 647 cannot be imaged with the fast routine and that adapting the photophysical properties of the dyes through chemical designing is necessary to further improve the localization speed in MINFLUX.

3. Conclusion

We present a new strategy to accelerate the localization process in a MINFLUX microscope up to 30-fold, compared with established strategies. Biomolecular-size localization precisions were achieved, with only a small trade-off produced by an increase of the scanning range (L). Despite a large reduction in the scanning times, only a moderate increase in excitation power (twofold) was necessary to compensate and collect a sufficient

number of photons. The general lack of fluorescent switches with blinking on-times in the millisecond range (1–3 ms), prompted the need of design specific markers to achieve our goal. To simplify the task, we selected dyes based on a stochastic blinking mechanism, avoiding more complex photo-induced mechanisms requiring the aid of additives or that may result in undesired excitation/activation cross-talk reactions. Our design builds upon a red-emitting silicon rhodamine core with a modified thiophene- or a benzothiophene-fused spirolactam fragment enabling the optimization by chemical modifications of the pendant *N*-aromatic amide substituent. Together, these modifications yielded a system independent of activation light schemes and buffer compositions (except pH values), working with a single laser in the red region (640 nm). We performed a systematic characterization of a series of stochastic blinking labels at the single molecule level, mimicking the conditions experienced while imaging in a MINFLUX microscope. We observed variations of the photophysical behavior of the dyes according to the type of chemical and biomolecular tags used, as well as a notable non-exponential behavior of the on-times affecting duty cycle distributions. With all the six tested fluorophores, imaging using coordinate-stochastic super-resolution methods was possible in fixed cells, and HaloTag ligands were found suitable for live-cell labeling. Remarkably, the new blinking fluorophores afforded considerably shorter on-times (over an order of magnitude) compared to those afforded by most blinking fluorophores reported in the literature. With the best fluorophore candidate, MINFLUX microscopy with down to 2.3 nm localization precision was achieved using a HaloTag ligand and anti-GFP nanobodies labeled with a hydrophilized thiol-reactive maleimide derivative. With only a small trade-off in precision (3.7 nm) with respect to previous work, namely by a factor of 4, we accelerated the localization on a commercial MINFLUX instrument up to 30-fold. This work emphasizes the benefits to be gained from meaningfully adapting procedures and rationally designed markers to the specific needs of a system, albeit the nanoscopy approach or the imaging target.

4. Experimental Section

General Methods: Absorption and emission spectra as a function of pH were measured with a CLARIOstar Plus microplate reader (BMG LABTECH GmbH, Germany) in 96-well non-binding polystyrene F-bottom, μClear microplates (200 μL per well; Greiner Bio-One GmbH, Ref. 655 906) at 25 °C in air-saturated solutions in triplicates. For determination of pK_{a1} and pK_{a2} values, plots of the $A^{\lambda max}$ (absorption at λ_{MAX} in the visible range) versus pH were fitted to the following equation

$$A^{\lambda_{max}} = A_{max} + (A_{max} - A_{min}) \times \left[\frac{1}{1 + 10^{(n_1 \times (pKa_1 - pH))}} + \frac{1}{1 + 10^{(n_2 \times (pH - pKa_2))}} \right] \quad (1)$$

where A_{max} and A_{min} are the limiting amplitude values, $K_{a1,2}$ the equilibrium constants, and $n_{1,2}$ the corresponding Hill's coefficients.

Fluorescence quantum yields were obtained with a Quantaurus-QY absolute PL quantum yield spectrometer (model C11347-11, Hamamatsu) according to the manufacturer's instructions.

Protein Labeling: Polyclonal antibodies (goat anti-rabbit IgG [H + L], Table 1) were labeled using a standard procedure.[65] The pH of 2 mg mL^{-1} protein solutions was adjusted to ≈8.0 with a 1 M sodium bicarbonate solution and stirred for 1 h at r.t. with 10 equiv. of the

**ADVANCED
SCIENCE NEWS**

www.advancedsciencenews.com

**NANO · MICRO
small**

www.small-journal.com

corresponding NHS ester (for STORM imaging), or 1 equiv. (for single molecule experiments). The mixture was purified using size-exclusion chromatography (PD MidiTrap G-25, GE Healthcare Bio-Sciences, gravity protocol) and stored at 4 °C. The degree of labeling (DOL) obtained was calculated from spectrophotometric measurements as ≈2–3, for the concentrated mixtures, and estimated as ≈0.2–0.3 for the diluted mixtures from the reactive ratios. Anti-GFP nanobodies were labeled with compound **4**-Maleimide using a previously described protocol, and the DOL corroborated by mass spectrometry (Figure S10A, Supporting Information). Binding of the HaloTag ligand derived from compound **4** in vitro was corroborated by mass spectrometry (Figure S10B, Supporting Information). The dye was diluted to 1 μM with PBS and mixed with 1.05 equiv. of the protein, incubated for 2 h at r.t., and submitted for mass spectrometry analysis.

Single Molecule Samples: Samples were prepared by a modified procedure (Figure S3, Supporting Information), based on reported immobilization methods.[66,67] Flow chambers were constructed by attaching an oxygen plasma cleaned coverslip to an objective slide with double-sided adhesive tape. The chamber was incubated with PLL-PEG-biotin (0.2 mg mL^{-1}) and Tween-20 (1% v/v) in ddH$_2$O for 15 min, incubated with Streptavidin (10 μg mL^{-1}) in PBS for 5 min, incubated with biotinylated polyclonal antibody (≈10 μg mL^{-1}) from rabbit for 5 min, incubated with dye-labeled polyclonal anti-rabbit antibody (≈10 μg mL^{-1}) for 5 min, and filled with PBS for measurements (rinsing with PBS between individual steps). For HaloTag assays, the same chambers were incubated with PLL-PEG-NTA (0.2 mg mL^{-1}) and Tween-20 (1% v/v) in ddH$_2$O for 15 min, incubated with NiCl$_2$ (2 μg mL^{-1}) for 5 min, incubated with his-tagged HaloTag7 (≈0.5 μM), incubated with HaloTag ligand of the corresponding dye (10 nM), and filled with PBS for measurements (rinsing with PBS between individual steps). The used reagents are summarized in Table S4, Supporting Information.

Cell Culture and Fluorescence Labeling: COS-7, HK-2xZFN-mEGFP-Nup107 (CLS GmbH, 300 676) and U2OS-Vim-Halo cells were cultured in Dulbecco's modified Eagle medium (DMEM, 4.5 g L^{-1} glucose) in a CO$_2$ incubator humidified at 5% at 37 °C. The medium contains GlutaMAX and sodium pyruvate (ThermoFisher 31 966), and supplemented with 10% v/v fetal bovine serum (FBS, ThermoFisher 10 500 064) and 1% penicillin–streptomycin (Gibco 15 140 122). U2OS-Nup96-Halo (CLS GmbH, 300 448) and U2OS-ZFN-Snap-Nup107 (CLS GmbH, 300 294) cells were cultured in McCoy's 5A medium (Gibco 26 600 023) in a CO$_2$ incubator at 37 °C humidified to 5%. The medium contains L-glutamine and sodium pyruvate and is supplemented with 10% v/v FBS (ThermoFisher 10 500 064) and 1% penicillin–streptomycin (Gibco 15 140 122). The cells were plated on glass coverslips for 24–48 h prior to fixing or labeling.

Halo cell lines were labeled live with the HaloTag ligands (250 nM) for 24 h in the corresponding medium, and washed twice with medium for at least 1 h. For live-cell imaging, samples were mounted in FluoBrite (Invitrogen) supplemented with 10% FBS (ThermoFisher) and 2% GlutaMAX (Gibco). For fixed-cell imaging (U2OS-Nup96-Halo), samples were washed with PBS, and fixed with PFA (3%) at room temperature for 20 min, quenched with 0.1 M NH$_4$Cl and 0.1 M glycine in PBS (QB) for 10 min, permeabilized with Triton X-100 0.1% in PBS for 5 min and washed twice with PBS (5 min). For counter-labeling, they were stained with WGA AF488 in PBS and washed twice with PBS. mEGFP cells were fixed, permeabilized, and blocked according to a reported protocol,[53,68] and labeled with the self-blinking nanobody conjugate for 60 min at r.t. Nup-Snap cells were fixed and labeled according to a reported protocol.[16] COS-7 cells were washed with PBS, fixed for 5 min with MeOH cooled to −20 °C, rinsed twice with PBS and blocked with BSA (2%) for 45–60 min. Cells were incubated with a primary rabbit antibody against α-tubulin for 60 min at r.t. (or overnight at 4 °C) in BSA, washed twice with BSA for 5 min, and then incubated with the anti-rabbit conjugate of the dye of interest in BSA for 60 min at r.t. Afterward samples were washed with BSA, then twice with PBS.

All fixed samples were mounted on a concave coverslide filled with PBS, and sealed with a two-component silicon resin (Picodent Twinsil, Picodent Dental-Produktions- und Vertriebs-GmbH). Details

on the used antibodies, nanobodies, and proteins are summarized in Table S5, Supporting Information. Samples stained with Alexa Fluor 647 were mounted on a concave coverslide filled with a blinking buffer system containing 50 mM Tris-HCl (pH = 8.0), 10% wt/vol glucose, 10 mM NaCl, 10 mM MEA (cysteamine hydrochloride), 66 μg mL^{-1} catalase, and 0,4 mg mL^{-1} pyranose oxidase.

Single Molecule Characterization Setup: Characterization was performed in a custom-built microscope setup that can be switched between wide-field and confocal mode. A scheme with a more detailed description can be found in Figure S15, Supporting Information. The microscope was equipped with a laser for excitation at 642 nm (MPB Communications, P_{max} = 1000 mW) and a laser for optional activation at 405 nm (Cobolt MLD-06, Hübner). The sample was placed on a custom-built stage based on a 3 degrees of freedom piezo positioning system (XYZ-SLC1740, SmarAct), which is built on a commercial Leica DMi8 (Leica Microsystems, Wetzlar, Germany) microscope. Illumination of the samples in both modes is done through a Leica HCX PL APO NA 1.46 Oil corrected objective lens. For wide-field detection an EMCCD camera was used (iXon DVU897, Andor Oxford Instruments, Abingdon UK), which detects light according to the filters built in the microscope body (Semrock HC 660 and Chroma ET700/75). For confocal detection, emission light was focused onto an avalanche photo diode (Excelitas SPCM-AQRH-13, Excelitas Technologies Corp. Waltham, USA), detecting light with a wavelength between 660 and 800 nm (Semrock 731/137 Brightline HC). The setup was controlled with a custom-written LabView software, which communicates with single components via a field programmable gate array board (FPGA, PCIe-R7852r, National Instruments, Austin, USA). Operating at a base clock frequency of 100 MHz, it allows real-time control of the data acquisition. Wide-field data was acquired with the aid of the software provided by the camera manufacturer (Andor Solis), which interacts with the LabView software.

Single Molecule Data Analysis: Single molecule data was acquired with any of the two illumination techniques described above and analyzed with custom-written MATLAB (MathWorks, USA) scripts. Separation of the signal from the noise was done by setting first an approximated threshold well above the background noise. Then, the signal below this threshold was fitted with a Gaussian (wide-field measurements) or a Poissonian (confocal measurements) distribution function. A final threshold was calculated excluding 99 999% (Gaussian distribution) and 99 994% (Poissonian distribution) of the noise. Then, single molecule traces were binarized using that threshold and most relevant parameters were calculated from the binary curves (e.g., T_{ON}, T_{OFF}, DC, N_C), except frequencies, total photons, and photons per cycles, which were calculated from the product of the trace and its binarized trace. Figure S5, Supporting Information, shows a scheme visualizing the used method. The number of cycles (N_C) was obtained by counting the number of positive flanks in the binary trace. The total number of photons (N_{PH}) was calculated as the sum of counts of the product of the trace and its binarized trace. The mean value of photons per cycle (PH_{CY}) was calculated from the ratio of the previous values (N_{PH}/N_C). To evaluate average on- and off-times, the histogram of all calculated events was plotted (Figures S5–S7, Supporting Information) and fitted to either a mono-exponential function (T_{OFF}) or a bi-exponential function (T_{ON}). The average photon rate can be obtained by dividing the photons/event (PH_{Cy}) through the duration of the event (T_{ON}).

STORM Imaging: STORM images were acquired on the setup described for single molecule characterization, on the wide-field mode, but excitation was performed with HILO ("highly inclined and laminated optical sheet microscopy"[69]). Typically, 5000 frames for live-cell images, and 30 000 frames for fixed cells were recorded. The frame rates used were 50 Hz for fixed-cell (20 ms per frame) and 200 Hz for live-cell (5 ms per frame) imaging. Data analysis was performed using ThunderSTORM ImageJ plugin,[70] including data merging and drift correction. Data was further filtered for outliers based on the sigma parameter (localization Gaussian fitting) and the uncertainty, and rendered by a custom-written MATLAB script. The images were rendered as Gaussians with a fixed size corresponding to the mean uncertainty of the localizations.

2206026 (9 of 11)

ADVANCED
SCIENCE NEWS

www.advancedsciencenews.com

NANO · MICRO
small

www.small-journal.com

MINFLUX Imaging: MINFLUX images were acquired on a commercial Abberior 3D MINFLUX microscope, equipped with a 560 and a 640 nm (cw) excitation laser line. The system also contains a 488 nm laser line only for confocal imaging, and a 405 nm laser for activation. In our measurements, only the excitation line at 640 nm was used. Detection was performed in two channels with the ranges 650–685 and 685–720 nm, respectively; signal from both channels was added up. The system is also equipped with a real-time position stabilization system, based on an infrared laser (975 nm) and a wide-field detection system of the light scattered at the sample interface. Image acquisition was done with different excitation powers starting from 240–540μW (in front of the scanner) at the MINFLUX localization step. Different distances (L) for the last MINFLUX step have been taken depending of the aim of the measurement. Two imaging sequences were used for imaging, the standard (slow) and the optimized (fast) one. Table S3, Supporting Information, summarizes the main steps and imaging parameters.

Image and data post-processing was performed by custom-built MATLAB routines, described previously.[34] Briefly, the data was first filtered with a density-based clustering algorithm (DBSCAN, epsilon = 4–8 nm, minPts = 3). Then, events with low emission frequency (<35–55 kHz depending on the sequence), with outside–inside ratio (CFR) of the photon count outside the range −0.5–0.8, and with less than two localizations were filtered out. Negative CFR values were assumed to come from center frequencies that were slightly below the average background level. A second filter was applied based on the spread of the localizations around their mean value. The distribution was first fitted with a 2D-Gaussian function, and localizations lying outside a radius corresponding to 90% ($1.645 \times \sigma$) of the distribution were discarded. The images were then plotted via an amplitude-normalized Gaussian rendering (pixel-size = 1 nm) with fixed sigma ($\sigma_X = \sigma_Y$) as the average value from the distribution of all remaining (filtered) molecules. For visualization purposes (the number of localizations varies with on-time and number of cycles) the color maps used in the images are non-linear with a gamma correction of $A = 1$ and $\gamma = 0.5$. We further extracted the number of photons per localization, the total number of photons from a trace (N_{PH}, including the pre-localization and all localizations), and the localization time (T_{LOC}) calculated from the difference in time-stamp of its last and first localizations. The mean, the median, and the expectation value (τ) from a mono-exponential fit of the distributions (histogram) of each variable were calculated.

Supporting Information

Supporting Information is available from the Wiley Online Library or from the author.

Conflict of Interest

S.W.H. is a co-founder of the company Abberior Instruments which commercializes MINFLUX microscopes. S.W.H. also holds patents on the principles, embodiments and procedures of MINFLUX through the Max Planck Society.

Author Contributions

A.N.B. and M.L.B. were responsible for the project's conception. M.L.B. and M.R. wrote the manuscript with input from A.N.B. and S.W.H. A.N.B. performed the chemical synthesis; M.R., L.S., M.L.B., and A.N.B. performed dye characterization; M.R. and M.L.B. performed labeling, microscopy, and data analysis; S.W.H. directed and supervised the investigations; all the authors discussed the results and commented on the manuscript.

Data Availability Statement

The data that support the findings of this study are available from the corresponding author upon reasonable request.

[1] S. W. Hell, *Science* **2007**, *316*, 1153.
[2] S. W. Hell, J. Wichmann, *Opt. Lett.* **1994**, *19*, 780.
[3] M. Hofmann, C. Eggeling, S. Jakobs, S. W. Hell, *Proc. Natl. Acad. Sci. U. S. A.* **2005**, *102*, 17565.
[4] E. Betzig, G. H. Patterson, R. Sougrat, O. W. Lindwasser, S. Olenych, J. S. Bonifacino, M. W. Davidson, J. Lippincott-Schwartz, H. F. Hess, *Science* **2006**, *313*, 5793.
[5] S. T. Hess, T. P. K. Girirajan, M. D. Mason, *Biophys. J.* **2006**, *91*, 4258.
[6] M. J. Rust, M. Bates, X. Zhuang, *Nat. Methods* **2006**, *3*, 793.
[7] A. Sharonov, R. M. Hochstrasser, *Proc. Natl. Acad. Sci. USA* **2006**, *103*, 18911.
[8] S. J. Sahl, S. W. Hell, S. Jakobs, *Nat. Rev. Mol. Cell Biol.* **2017**, *18*, 685.
[9] F. Balzarotti, Y. Eilers, K. C. Gwosch, A. H. Gynnå, V. Westphal, F. D. Stefani, J. Elf, S. W. Hell, *Science* **2016**, *355*, 606.
[10] S. D. Gallegos-Cerda, J. D. Hernández-Varela, J. J. Chanona-Pérez, B. Arredondo Tamayo, J. V. Méndez Méndez, *Food Bioprocess Technol.* **2022**, 1.
[11] M. Bates, B. Huang, G. T. Dempsey, X. Zhuang, *Science* **2007**, *317*, 1749.
[12] Y. Li, W. Shi, S. Liu, I. Cavka, Y. Wu, U. Matti, D. Wu, S. Koehler, J. Ries, *Nat. Commun.* **2022**, *13*, 3133.
[13] J. B. Grimm, T. Klein, B. G. Kopek, G. Shtengel, H. F. Hess, M. Sauer, L. D. Lavis, *Angew. Chem., Int. Ed.* **2016**, *55*, 1723.

ADVANCED
SCIENCE NEWS

www.advancedsciencenews.com

NANO · MICRO

small

www.small-journal.com

[14] J. K. Pape, T. Stephana, F. Balzarotti, R. Büchner, F. Lange, D. Riedel, S. Jakobs, S. W. Hel, *Proc. Natl. Acad. Sci. USA* **2020**, *117*, 20607.

[15] K. C. Gwosch, J. K. Pape, F. Balzarotti, P. Hoess, J. Ellenberg, J. Ries, S. W. Hell, *Nat. Methods* **2020**, *17*, 217.

[16] R. Schmidt, T. Weihs, C. A. Wurm, I. Jansen, J. Rehman, S. J. Sahl, S. W. Hell, *Nat. Commun.* **2021**, *12*, 1478.

[17] A. N. Butkevich, M. Weber, A. R. C. Delgado, L. M. Ostersehlt, E. D'Este, S. W. Hell, *J. Am. Chem. Soc.* **2021**, *143*, 18388.

[18] Y. Eilers, H. Ta, K. C. Gwosch, F. Balzarotti, S. W. Hell, *Proc. Natl. Acad. Sci. U. S. A.* **2018**, *115*, 6117.

[19] M. Heilemann, E. Margeat, R. Kasper, M. Sauer, P. Tinnefeld, *J. Am. Chem. Soc.* **2005**, *127*, 3801.

[20] G. T. Dempsey, J. C. Vaughan, K. H. Chen, M. Bates, X. Zhuang, *Nat. Methods* **2011**, *8*, 1027.

[21] C. Steinhauer, C. Forthmann, J. Vogelsang, P. Tinnefeld, *J. Am. Chem. Soc.* **2008**, *130*, 16840.

[22] N. C. Goossen-Schmidt, M. Schnieder, J. Hüve, J. Klingauf, *Sci. Rep.* **2020**, *10*, 13746.

[23] N. Olivier, D. Keller, V. S. Rajan, P. Gönczy, S. Manley, *Biomed. Opt. Express* **2013**, *4*, 885.

[24] X. Shi, J. Lim, T. Ha, *Anal. Chem.* **2010**, *82*, 6132.

[25] G. T. Dempsey, M. Bates, W. E. Kowtoniuk, D. R. Liu, R. Y. Tsien, X. Zhuang, *J. Am. Chem. Soc.* **2009**, *131*, 18192.

[26] Y. Gidi, L. Payne, V. Glembockyte, M. S. Michie, M. J. Schnermann, G. Cosa, *J. Am. Chem. Soc.* **2020**, *142*, 12681.

[27] V. N. Belov, C. A. Wurm, V. P. Boyarskiy, S. Jakobs, S. W. Hell, *Angew. Chem., Int. Ed.* **2010**, *49*, 3520.

[28] H. D. Lee, S. J. Lord, S. Iwanaga, K. Zhan, H. Xie, J. C. Williams, H. Wang, G. R. Bowman, E. D. Goley, L. Shapiro, R. J. Twieg, J. Rao, W. E. Moerner, *J. Am. Chem. Soc.* **2010**, *132*, 15099.

[29] S. Banala, D. Maurel, S. Manley, K. A. C. Johnsson, *ACS Chem. Biol.* **2012**, *7*, 289.

[30] S. Hauke, A. von Appen, T. Quidwai, J. Ries, R. Wombacher, *Chem. Sci.* **2017**, *8*, 559.

[31] M. S. Frei, P. Hoess, M. Lampe, B. Nijmeijer, M. Kueblbeck, J. Ellenberg, H. Wadepohl, J. Ries, S. Pitsch, L. Reymond, K. Johnsson, *Nat. Commun.* **2019**, *10*, 4580.

[32] Y. Zheng, Z. Ye, Z. Liu, W. Yang, X. Zhang, Y. Yang, Y. Xiao, *Anal. Chem.* **2021**, *93*, 7833.

[33] R. Lincoln, M. L. Bossi, M. Remmel, E. D'Este, A. N. Butkevich, S. W. Hell, *Nat. Chem.* **2022**, *14*, 1013.

[34] A. N. Butkevich, M. L. Bossi, G. Lukinavičius, S. W. Hell, *J. Am. Chem. Soc.* **2019**, *141*, 981.

[35] G. Lukinavičius, K. Umezawa, N. Olivier, A. Honigmann, G. Yang, T. Plass, V. Mueller, L. Reymond, I. R. CorrêaJr., Z.-G. Luo, C. Schultz, E. A. Lemke, P. Heppenstall, C. Eggeling, S. Manley, K. Johnsson, *Nat. Chem.* **2013**, *5*, 132.

[36] S. Uno, M. Kamiya, T. Yoshihara, K. Sugawara, K. Okabe, M. C. Tarhan, H. Fujita, T. Funatsu, Y. Okada, S. Tobita, Y. Urano, *Nat. Chem.* **2014**, *6*, 681.

[37] H. Takakura, Y. Zhang, R. S. Erdmann, A. D. Thompson, Y. Lin, B. McNellis, F. Rivera-Molina, S. Uno, M. Kamiya, Y. Urano, J. E. Rothman, J. Bewersdorf, A. Schepartz, D. Toomre, *Nat. Biotechnol.* **2017**, *35*, 773.

[38] S. Uno, M. Kamiya, A. Morozumia, Y. Urano, *Chem. Commun.* **2018**, *54*, 102.

[39] Q. Qi, W. Chi, Y. Li, Q. Qiao, J. Chen, L. Miao, Y. Zhang, J. Li, W. Ji, T. Xu, X. Liu, J. Yoon, Z. Xu, *Chem. Sci.* **2019**, *10*, 4914.

[40] Q. Zheng, A. X. Ayala, I. Chung, A. V. Weigel, A. Ranjan, N. Falco, J. B. Grimm, A. N. Tkachuk, C. Wu, J. Lippincott-Schwartz, R. H. Singer, L. D. Lavis, *ACS Cent. Sci.* **2019**, *5*, 1602.

[41] R. Tachibana, M. Kamiya, A. Morozumi, Y. Miyazaki, H. Fujioka, A. Nanjo, R. Kojima, T. Komatsu, T. Ueno, K. Hanaoka, T. Yoshihara, S. Tobita, Y. Urano, *Chem. Commun.* **2020**, *56*, 13173.

[42] P. Werther, K. Yserentant, F. Braun, N. Kaltwasser, C. Popp, M. Baalmann, D.-P. Herten, R. Wombacher, *Angew. Chem., Int. Ed.* **2020**, *59*, 804.

[43] P. M. Pereira, N. Gustafsson, M. Marsh, M. M. Mhlanga, R. Henriques, *Traffic* **2020**, *21*, 375.

[44] A. Morozumi, M. Kamiya, S. Uno, K. Umezawa, R. Kojima, T. Yoshihara, S. Tobita, Y. Urano, *J. Am. Chem. Soc.* **2020**, *142*, 9625.

[45] N. Lardon, L. Wang, A. Tschanz, P. Hoess, M. Tran, E. D'Este, J. Ries, K. Johnsson, *J. Am. Chem. Soc.* **2021**, *143*, 14592.

[46] Q. Qiao, W. Liu, J. Chen, X. Wu, F. Deng, X. Fang, N. Xu, W. Zhou, S. Wu, W. Yin, X. Liu, Z. Xu, *Angew. Chem., Int. Ed.* **2022**, *61*, e202202961.

[47] J. Tyson, K. Hu, S. Zheng, P. Kidd, N. Dadina, L. Chu, D. Toomre, J. Bewersdorf, A. Schepartz, *ACS Cent. Sci.* **2021**, *7*, 1419.

[48] R. Gerasimaitė, J. Bucevičius, K. A. Kiszka, S. Schnorrenberg, G. Kostiuk, T. Koenen, G. Lukinavičius, *ACS Chem. Biol.* **2021**, *16*, 2130.

[49] H. Shroff, C. G. Galbraith, J. A. Galbraith, E. Betzig, *Nat. Methods* **2008**, *5*, 417.

[50] L. D. Lavis, *Annu. Rev. Biochem.* **2017**, *86*, 825.

[51] J. Fölling, V. Belov, R. Kunetsky, R. Medda, A. Schönle, A. Egner, C. Eggeling, M. Bossi, S. W. Hell, *Angew. Chem., Int. Ed.* **2007**, *46*, 6266.

[52] M. Bossi, J. Fölling, V. N. Belov, V. P. Boyarskiy, R. Medda, A. Egner, C. Eggeling, A. Schönle, S. W. Hell, *Nano Lett.* **2008**, *8*, 2463.

[53] S. Uno, M. Kamiya, A. Morozumia, Y. Urano, *Chem. Commun.* **2018**, *54*, 102.

[54] R. Tachibana, M. Kamiya, A. Morozumi, Y. Miyazaki, H. Fujioka, A. Nanjo, R. Kojima, T. Komatsu, T. Ueno, K. Hanaoka, T. Yoshihara, S. Tobita, Y. Urano, *Chem. Commun.* **2020**, *56*, 13173.

[55] M. K. Lee, P. Rai, J. Williams, R. J. Twieg, W. E. Moerner, *J. Am. Chem. Soc.* **2014**, *136*, 14003.

[56] L. Wang, M. Tran, E. D'Este, J. Roberti, B. Koch, L. Xue, K. Johnsson, *Nat. Chem.* **2020**, *12*, 165.

[57] L. Yuan, W. Lin, Y. Feng, *Org. Biomol. Chem.* **2011**, *9*, 1723.

[58] S. G. Stratton, G. H. Taumoefolau, G. E. Purnell, M. Rasooly, W. L. Czaplyski, E. J. Harbron, *Chem. - Eur. J.* **2017**, *23*, 14064.

[59] G. V. Los, L. P. Encell, M. G. McDougall, D. D. Hartzell, N. Karassina, C. Zimprich, M. G. Wood, R. Learish, R. F. Ohana, M. Urh, D. Simpson, J. Mendez, K. Zimmerman, P. Otto, G. Vidugiris, J. Zhu, A. Darzins, D. H. Klaubert, R. F. Bulleit, K. V. Wood, *ACS Chem. Biol.* **2008**, *3*, 373.

[60] A. N. Butkevich, *Org. Lett.* **2021**, *23*, 2604.

[61] J. B. Grimm, T. A. Brown, A. N. Tkachuk, L. D. Lavis, *ACS Cent. Sci.* **2017**, *3*, 975.

[62] B. Roubinet, M. Bischoff, S. Nizamov, S. Yan, C. Geisler, S. Stoldt, G. Y. Mitronova, V. N. Belov, M. L. Bossi, S. W. Hell, *J. Org. Chem.* **2018**, *83*, 6466.

[63] J. V. Thevathasan, M. Kahnwald, K. Cieśliński, P. Hoess, S. K. Peneti, M. Reitberger, D. Heid, K. C. Kasuba, S. J. Hoerner, Y. Li, Y.-L. Wu, M. Mund, U. Matti, P. M. Pereira, R. Henriques, B. Nijmeijer, M. Kueblbeck, V. J. Sabinina, J. Ellenberg, J. Ries, *Nat. Methods* **2019**, *16*, 1045.

[64] M. Theiss, J.-K., Hériché, C. Russell, D., Helekal, A. Soppitt, J. Ries, J. Ellenberg, A. Brazma, V. Uhlmann, *bioRxiv* 2022.05.17.492295 **2022**.

[65] G. T. Hermanson, in *Bioconjugate Techniques*, 2nd ed., Elsevier, Amsterdam **2008**, p. 421.

[66] M. Zhao, P. R. Nicovich, M. Janco, Q. Deng, Z. Yang, Y. Ma, T. Böcking, K. Gaus, J. J. Gooding, *Langmuir* **2018**, *34*, 10012.

[67] G. Zhen, S. Zürcher, D. Falconnet, F. Xu, E. Kuennemann, M. Textor, in *IEEE Engineering in Medicine and Biology 27th Annual Conf.*, IEEE, Piscataway, NJ **2005**, 1036–1038.

[68] T. Pleiner, M. Bates, S. Trakhanov, C.-T. Lee, J. E. Schliep, H. Chug, M. Böhning, H. Stark, H. Urlaub, D. Görlich, *eLife* **2015**, *4*, 11349.

[69] M. Tokunaga, N. Imamoto, K. Sakata-Sogawa, *Nat. Methods* **2008**, *5*, 2.

[70] M. Ovesný, P. Křížek, J. Borkovec, Z. Švindrych, G. M. Hagen, *Bioinformatics* **2014**, *16*, 2389.

2206026 (11 of 11)